PROCEEDINGS, 43rd Workshop on Geothermal Reservoir Engineering
Stanford University, Stanford, California, February 12-14, 2018
SGP-TR-213

Variational Parallel Information Transfer between Unstructured Grids in Geophysics - Applications and Solutions Methods

Cyrill Planta[1], Daniel Vogler[2,3], Maria Nestola[1], Patrick Zulian[1], Rolf Krause[1]

[1]Institute of Computational Science, USI, Via Giuseppe Buffi 13, 6900, Lugano Switzerland
[2]Institute of Geophysics, ETH Zurich, Sonneggstr. 5, 8092 Zurich, Switzerland
[3]Institute of Process Engineering, ETH Zurich, Sonneggstr. 3, 8092 Zurich, Switzerland

cyrill.von.planta@usi.ch

Keywords: Variational transfer, L^2-projection, contact problem, fluid structure interaction, multigrid

ABSTRACT

State of the art simulations of enhanced geothermal systems are multi-physics simulations, where different physical properties are often being modeled on different geometries or grids. For example, for the simulation of fluids many prefer finite difference or volume formulations on structured grids, whereas in mechanics finite element formulations on unstructured grids are often preferred. To transfer information between these various geometries, we use a generic variational transfer operator, which has previously been introduced as pseudo-L^2-projection.

In this paper, we demonstrate that this transfer operator can be particularly useful for geophysics with three applications: First, in contact simulations we often have non-matching surfaces at the contact boundary. Here, the transfer operator acts as a mortar projection and we show with high resolution rock fracture geometries from the Grimsel Test Site in Switzerland how the variational transfer operator is used to formulate the contact problem. Secondly, we present a three-dimensional fluid-structure simulation, computing water flow between two rock surfaces and simultaneous deformation with an immersed boundary approach. In this method the solid, which is formulated on an unstructured grid, interacts with the fluid, formulated on a structured grid, by means of weakly enforced velocity constraints at the interface between fluid and solid. And lastly, we show how the transfer operator can be used to effectively solve contact problem between rock bodies. Using our operator, we can generate nested multilevel hierarchies, enabling us to solve the problem with optimal complexity, thus extending the possible size of simulations immensely.

1 INTRODUCTION

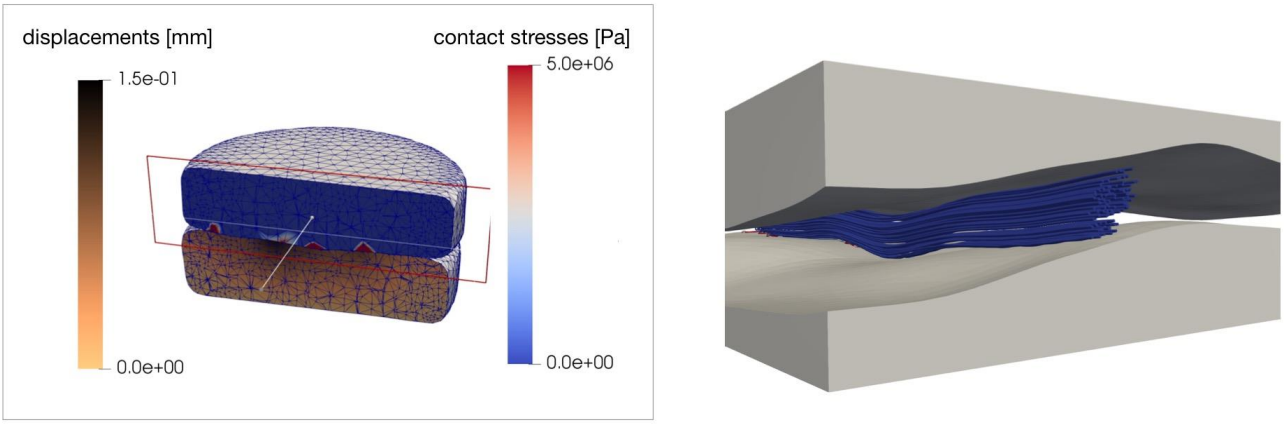

Figure 1: Left: Contact simulation between two rocks with nonmatching surfaces. In blue-red are the contact stresses, the displacement of the lower body is visualized in brown colors. Right: Fluid flow through fracture. The fluid is simulated in a uniform grid, whereas the solid fracture is modelled with an unstructured grid.

The mechanical and hydro-mechanical (HM) behavior of rock fractures strongly influences reservoir engineering applications, such as enhanced geothermal systems (EGS) and CO_2 sequestration (Rutqvist and Stephansson 2003; Tester et al. 2006). Here, the (hydro-) mechanical fracture behavior can dominate both economic efficiency and risk (e.g., induced seismic hazards) of the respective application (McClure and Horne 2014). An extensive body of literature has therefore studied rock fractures for their surface properties (Bandis, Lumsden, and Barton 1983; Zangerl et al. 2008; Vogler et al. 2017), and the relationship between fracture surfaces and mechanical (Bandis, Lumsden, and Barton 1983; Barton, Bandis, and Bakhtar 1985; Yu and Vayssade 1991; Pyrak-Nolte and Morris 2000; Jiang, Li, and Tanabashi 2006; Matsuki et al. 2008; Tatone and Grasselli 2015) and hydraulic behavior (Brown 1987; Zimmerman, Kumar, and Bodvarsson 1991; Nemoto et al. 2009; Park et al. 2013; Vogler et al. 2016).

Specifically, rock strength, fracture surface topography and the corresponding fracture contact area determine the fracture response to normal or shear loading. During normal loading, fracture closure commonly shows a strongly non-linear behavior, as increasing contact area decreases fracture compliance (Bandis, Lumsden, and Barton 1983; Matsuki et al. 2008; Zangerl et al. 2008; Vogler et al. 2016, 2018).

Naturally, mechanical deformation and the corresponding change in contact area and aperture field have a significant impact on fluid flow in fractures. As fractures close with increasing normal stresses, the total aperture area (i.e., gap between fracture surfaces) available for flow decreases, and flow patterns become increasingly tortuous and flow path channeling emerges (Brown 1987; Nemoto et al. 2009; Vogler et al. 2018). Additionally, fracture closure can lead to a significant increase of fluid pressure, which counteracts mechanical forces closing the fracture. Thus, the relationship between fracture closure and fluid pressure and respective fluid flow fields is tightly coupled. For geothermal energy production, high pressure fluid injection aims to open fractures to achieve higher fluid flow and heat extraction rates, while CO_2 sequestration tries to minimize fluid flow out of the reservoir along high permeability structures such as fractures. Predicting HM processes in fractures is challenging, as fractures commonly have complex geometries with surface roughness on the millimeter scale, and the previously mentioned strongly non-linear behavior for mechanical and HM processes. Investigation of HM fracture processes by numerical simulation is therefore computationally expensive, and most numerical and analytical studies rely on simplifying assumptions (Barton, Bandis, and Bakhtar 1985; Nemoto et al. 2009).

From a numerical perspective we characterize the fractured rock as a multi body contact problem. Using a finite element formulation of linear elasticity to describe the rock domains, the main difficulties lie in the formulation of the proper contact constraints between the rock surfaces, which have usually non-matching grids at the possible contact boundaries. Furthermore, the solution of the contact problem gives rise to a nonlinear problem, which, trying to describe rough rock surfaces on millimeter scales and below, may have millions of degrees of freedom and more. When simulating fluid and solid domain together, the "natural" formulation for fluid behavior is usually in Eulerian coordinates with structured grids, whereas for solid mechanics Lagrangian coordinates and corresponding unstructured grids are preferred. This leads to the issue of coupling the physical properties between different solution spaces.

In this work, we show how one can use variational transfer operators, which we call L^2-, or pseudo L^2- projections in the following, to address these issues. After introducing the L^2-projection, we show, following Wohlmuth and Krause (2003), how they can be used to resolve the contact conditions at the boundaries between the rock surfaces. Next, we show the coupling of the solid and fluid domain in fluid-structure-interaction (FSI) simulations with an immersed boundary method, which we have adapted from Nestola et al. (2017). Lastly, we will use L^2-projections to construct a nested hierarchy of fine-to-coarse spaces. We combine the semigeometric multigrid from Dickopf and Krause (2009) with the nonsmooth multilevel method from Kornhuber and Krause (2001 and to solve contact problems on complex fracture geometries with multigrid efficiency and without the need for regularization techniques such as the penalty or augmented Lagrangian methods.

All applications of the L^2-projection together allow us, to set up scalable finite element simulations of contact and fluid flow in fractures with pure three-dimensional continuum mechanics formulations in supercomputing environments. We will present simulations with actual granodiorite rock specimen taken from the Grimsel test site in Switzerland and show how our approaches work with complex real-world geometries.

2 METHODS

In the following sections we introduce the L^2-projection and three applications. L^2-projections map functions from one function space V to another space W. Their appeal is their versatility: With three different choices for the function spaces V and W we get three applications. For the contact problem in Section 2.2 we map between trace spaces at the contact boundary. In the FSI simulation in Section 2.3 we map between the different finite element formulations of the fluid and the solid and in Section 2.4 we map from finer to coarser solution spaces of the solid problem to construct a nested multilevel hierarchy.

2.1 Variational transfer with L^2-projections

L^2-projections map functions from one function space V to another space W. For a well-defined L^2-projection it suffices that both spaces are subspaces of the same L^2-space, i.e. they share the same domain Ω and L^2-scalar product. The projection is then defined as the mapping $P: V \to W$, such that the difference is weakly zero for all $u \in W$:

$$(\mathrm{Pu} - \mathrm{u}, \mathrm{v})_{\mathrm{L}^2} = \int_\Omega (\mathrm{Pu} - \mathrm{u})\mathrm{v}\ \mathrm{d}\omega = 0,\ \forall \mathrm{v} \in \mathrm{W}. \tag{1}$$

For finite element simulations we need a matrix representation T of P. $V$and W are then finite dimensional spaces with discrete basis $(\lambda_i^\beta)_{i=1,\dots,\dim(\beta)}$, $\beta \in \{V, W\}$. We write the elements $u \in V$, $Pu := w \in W$ and $v \in W$ in their respective basis representations $u = \sum_{i=1,\dots,n} f_i\, \lambda_i^V$, $w = \sum_{j=1,\dots,m} h_j\, \lambda_j^W$ and $v = \sum_{k=1,\dots,m} l_k\, \lambda_k^W$ and reformulate the weak equality (1) as

$$(Pu, v)_{L^2} = (u, v)_{L^2},\ \forall v \in W. \tag{2}$$

And using the corresponding basis representations we reformulate (2) to

$$(\textstyle\sum_{j=1,\dots,n} f_j\, \lambda_j^V, \lambda_k^{\mathrm{W}})_{L^2} = (\sum_{i=1,\dots,m} h_i\, \lambda_i^W, \lambda_k^W)_{L^2},\ \forall k = 1, \dots m. \tag{3}$$

With $d_{k_i} := (\lambda_i^W, \lambda_k^W)_{L^2} = \int_\Omega \lambda_i^W \lambda_k^W \, d\gamma$, $b_{k_j} := (\lambda_k^V, \lambda_j^W)_{L^2} = \int_\Omega \lambda_k^V \lambda_j^W \, d\gamma$, $D := (d_{k_i})_{k,i=1,\dots,n}$ and $T := (b_{k_j})_{k=1,\dots m, j=1,\dots,n}$ we get the discrete operator $T := D^{-1}B$. As it is convenient for us in our application to completely assemble T as a matrix, we require the inverse of D. The computation of the inverted matrix D can be computationally expensive, hence we choose, if possible, a subspace $W' \subset W$, which is spanned by biorthogonal basis functions $\lambda_l^{W'}$ that fulfill the biorthogonality condition

$$(\lambda_i^W, \lambda_j^{W'})_{L^2} = \int_\Omega \lambda_i^W \lambda_j^{W'} \, d\gamma = \delta_{ij}. \tag{4}$$

This way, the inverse of D is simply an inverted diagonal matrix. W' is also called Mortar space and in the case of biorthogonal basis functions, P is called pseudo-L^2-projection. Computing the entries $(\lambda_i^V, \lambda_j^W)_{L^2} = \int_{\mathrm{supp}(\lambda_i^V) \cap \mathrm{supp}(\lambda_i^W)} \lambda_i^V \lambda_j^W \, d\omega$ is nontrivial, especially in parallel computing environments where one needs to find suitable quadrature points in $\mathrm{supp}(\lambda_i^V) \cap \mathrm{supp}(\lambda_j^W)$. In this work, we use the library MOONoLith to obtain the quadrature points and we refer to Krause and Zulian (2016) for an in-depth description of the necessary procedures in parallel communication, load distribution etc.

For contact problems this means that we do no longer need matching grids as we can map between arbitrarily meshed contact boundaries. For geophysical applications in general, it means that we can transfer the solution on a mesh used for our solid mechanics to the solution on a mesh used for fluid flow computations, and vice versa. This allows for the combination of different modeling domains and their respective meshes, regardless of the respective mesh and mesh-element shape.

2.2 Contact Formulation

Analytically contact between two fractures constitutes a two-body contact problem. In this section, we introduce the formulation of the two-body contact problem and how we can use the L^2-projection as a mortar operator for the coupling of the non-penetration constraints between the two bodies. We use a simplified notation using the same symbols for variables in the strong formulation and the respective counterparts in the finite element discretizations. For the most part we follow the formulation in Krause (2009) and refer the reader to this article for more details on the appropriate function spaces.

Strong formulation

We consider a master body $\Omega_m \subset \mathbb{R}^3$ and a slave body $\Omega_s \subset \mathbb{R}^3$. The boundary Γ_α, $\alpha \in \{m, s\}$ of each body is composed into three disjoint sets: A Neumann boundary Γ_α^N, a Dirichlet boundary Γ_α^N and boundary where the possible contact occurs: Γ_α^C. The displacements u are separated into displacements on the master and the slave body such that $u := [u_m, u_s]$ (see also Figure 2).

The material of Ω_α is considered to be linear elastic. We use Hooke's tensor $(E_{ijml}^\alpha)^3$, $1 \le i, j, l, m \le 3$, to formulate the stresses σ given by Hooke's law, using the index $,_j$ to abbreviate derivatives with respect to x_j:

$$\sigma_{ij}(u^\alpha) = E_{ijml}^\alpha u_{l,m}^\alpha. \tag{5}$$

We make use of a linearized contact formulation, in which we assume that the bodies are close together, such that we can substitute the outer normal ν_s on Γ_s^C with $-\nu_m$ (see also Kikuchi and Oden 1988). At Γ_C we define point-wise a function $g: \mathbb{R}^3 \to \mathbb{R}$, which measures the width of the gap between the two solid bodies in the normal direction (i.e., aperture in geophysics). We define point-wise the jump $[u \cdot n] := u^s \cdot n^s + u^m \cdot n^m$ which is to be smaller than the gap g: i.e. $[u \cdot n] \le g$.

For the contact conditions we need stresses and displacements with respect to the outer normal direction n^α and similarly for tangential displacements with respect to the tangential direction T:

$$\begin{aligned} \sigma_n^\alpha &= n_i^\alpha \cdot \sigma_{ij}(u^\alpha) \cdot n_j^\alpha & u_n^\alpha &= u^\alpha \cdot n^\alpha, \\ \sigma_T^\alpha &= \sigma(u^\alpha) \cdot n^\alpha - \sigma_n \cdot n^\alpha & u_T^\alpha &= u^\alpha - u_n^\alpha \cdot n^\alpha. \end{aligned} \tag{6}$$

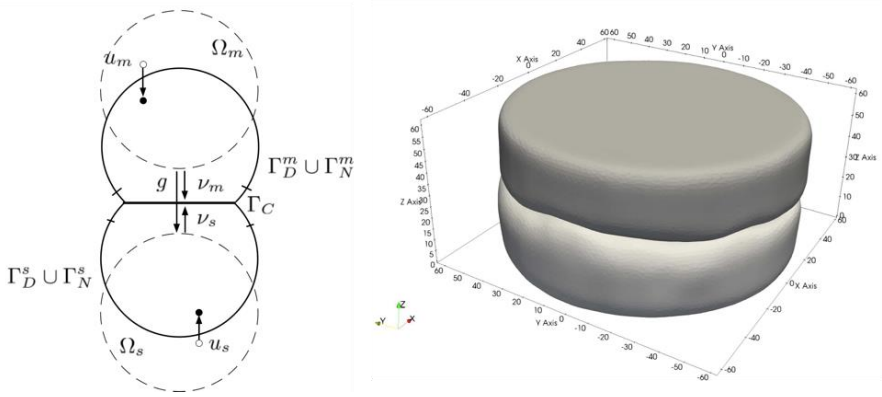

Figure 2: Left: classic setup of two body problem with spheres. Right: Contact between two meshed rock specimen with rough surfaces.

With this we can state the contact problem in the following form:

$$\begin{aligned} -\mathrm{div}\sigma(u) &= f \quad \text{in } \Omega_s \cup \Omega_m \\ u &= 0 \quad \text{on } \Gamma_D^\alpha \\ \sigma_{ij}(u) \cdot n_j &= p_i \quad \text{on } \Gamma_N^\alpha \\ \sigma_n &\leq 0 \quad \text{on } \Gamma_C. \end{aligned} \tag{7}$$

With contact conditions:

$$\begin{aligned} -\sigma_n(u^m) &= \sigma_n(u^s) \quad \text{on } \Gamma_C \\ [u \cdot n] &\leq g \quad \text{on } \Gamma_C \\ ([u \cdot n] - g)\sigma_n &= 0 \quad \text{on } \Gamma_C \\ \sigma_T &= 0 \quad \text{on } \Gamma_C. \end{aligned} \tag{8}$$

The second equation is the nonpenetration condition which make the initially linear elasticity problem nonlinear. The third equation are the complementary conditions and the last equation states that we have no stresses in tangential direction, i.e. we are considering frictionless contact.

2.2.1 Mortar coupling

For the Mortar coupling we define three index sets $\mathcal{M}, \mathcal{S}$ and $\mathcal{I}$ that label the nodes of the discretized finite element system arising from the contact problem. The indices of the nodes on the boundary Γ_m^C on the master side are in $\mathcal{M}$, those at the slave side in $\mathcal{S}$ and the indices of the remaining nodes in the interior are in $\mathcal{I}$. The Mortar projection is defined as the L^2-projection between the spaces defined on the master and the slave side of the contact boundary Γ^C, i.e. $P: \Gamma_m^C \to \Gamma_s^C$, such that

$$\int_{\Gamma^C} (Pu - u)v = 0, \ \forall v \in \mathcal{L} \subset H^{\frac{1}{2}}(\Gamma^C). \tag{9}$$

Note that the Mortar projection is defined on an appropriate subspace $\mathcal{L}$ of $H^{\frac{1}{2}}(\Gamma^C)$ on the boundary, which implies that for theoretical purposes it is assumed, that the two bodies are in contact and the displacements on the master and slave side only differ in their discretization. For a detailed introduction to the Mortar method and coupling we refer to Bernardi (1989), Bernardi et. al. (2005) and Wohlmuth and Krause (2003). Following the process outlined in 2.1 we get a discrete version $T = D^{-1}B$ of P, whereby we use a mortar space with biorthogonal basis functions. We then transform the system matrix $\widehat{A}$ of the finite element discretization in the following way:

$$A = \begin{bmatrix} Id & 0 & 0 \\ 0 & Id & T^t \\ 0 & 0 & Id \end{bmatrix} \begin{bmatrix} \widehat{A_{II}} & \widehat{A_{IM}} & \widehat{A_{IS}} \\ \widehat{A_{MI}} & \widehat{A_{MM}} & 0 \\ \widehat{A_{SI}} & 0 & \widehat{A_{SS}} \end{bmatrix} \begin{bmatrix} Id & 0 & 0 \\ 0 & Id & 0 \\ 0 & T & Id \end{bmatrix} \tag{10}$$

The idea behind this becomes clear, when one applies the operator T to the solution u:

$$\begin{bmatrix} Id & 0 & 0 \\ 0 & Id & 0 \\ 0 & T & Id \end{bmatrix} u = \begin{bmatrix} Id & 0 & 0 \\ 0 & Id & 0 \\ 0 & T & Id \end{bmatrix} \begin{bmatrix} u_I \\ u_M \\ u_S \end{bmatrix} = \begin{bmatrix} u_I \\ u_M \\ Tu_M + u_S \end{bmatrix} \tag{11}$$

On the third component we can thus apply a discretized version of the strong non-penetration condition $u^s \cdot n^s + u^m \cdot n^m = [u \cdot n] \leq g$. The transformed system is solvable by having constraints only on the third component of the transformed solution vector, for which we

can use solvers of the semismooth newton class (Hintermüller, Ito, and Kunisch 2002), or nonsmooth multilevel methods (Krause 2001, 2009; Dickopf and Krause 2009) as to be seen in Section 2.4.

2.3 Fluid Structure Interaction

Our approach for FSI follows the immersed boundary method (see for example Baaijens 2001, Hesch et al. 2014). We solve the fluid and solid problems on different grids and then use L^2-projections to transfer the velocities and pressure between the solid and the fluid grid. The fluid problem is coupled with the solid problem by enforcing a weak equality of the fluid and solid velocities in the overlapping regions. The solid problem is solved by adding a volume term, representing the force exerted from the fluid on the structure, which is recovered from the fluid pressure and velocity, in order to ensure the full coupling.

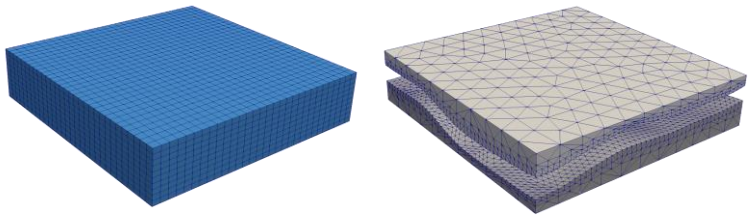

Figure 3: Left: Structured fluid grid. Right: unstructured solid grid

We use a standard Eulerian formulation for the Navier-Stokes equations for incompressible flow on the domain $\Omega_f \subset \mathbb{R}^3$ with a structured grid (see Figure 3 left) and a Lagrangian formulation for the elastic response of the rock on domain $\Omega_s \subset \Omega_f$ with an unstructured grid (see Figure 3 right). We denote with ρ_f the fluid density, with v_f the fluid velocity, with μ the dynamic viscosity and with u the position of the solid. In its strong formulation, the incompressible Navier Stokes problem is then given in the following form:

$$\begin{aligned} \rho_f \frac{\partial v_f}{\partial t} + \rho_f (v_f \cdot \nabla) v_f + \nabla p_f - \mu \,\triangle\, v_f &= 0 \qquad \text{on } \Omega_f \\ \nabla \cdot v_f &= 0 \qquad \text{on } \Omega_f \end{aligned} \tag{12}$$

For the elastodynamic problem with u as the displacement in the Lagrangian formulation, ρ_{s0} as the density of the solid, σ_s as the stress tensor and d as the external body force, the strong formulation reads as:

$$(\rho_{s0} - \rho_f)\frac{\partial^2 u}{\partial t^2} - \mathrm{div}\sigma_s(u) = 0 \qquad \text{on } \Omega_s \tag{13}$$

We define two L^2-projections P_s^f and $\widehat{P}_s^f$ to transfer fluid velocities and pressures to the solid problem. With $\hat{v}_f := P_s^f(v_f)$ we denote the image of v_f on the solid grid and with $\hat{p}_f := \hat{P}_s^f(p_f)$ the image of the fluid pressure. By choosing appropriate Mortar spaces W and $\widehat{W}$, we can then define the projections as in Section 2.1:

$$\int_{\Omega_f \cap \Omega_s} (\hat{v}_f - v_f)\delta v \, d\omega = 0, \ \forall\, \delta v \in W \quad \text{and} \quad \int_{\Omega_f \cap \Omega_s} (\hat{p}_f - p_f)\delta \hat{v} \, d\omega = 0, \forall\, \delta \hat{v} \in \widehat{W}. \tag{14}$$

With P_f^s, $v_s := P_f^s\left(\frac{\partial u}{\partial t}\right)$ and Mortar space V, we define the transfer the solid velocity back to the fluid:

$$\int_{\Omega_f \cap \Omega_s} (v_s - \frac{\partial u}{\partial t})\, \delta \dot{u} \, d\omega = 0, \ \forall\, \delta \dot{u} \in V. \tag{15}$$

The coupling itself is achieved by enforcing the following weak equality:

$$\int_{\Omega_f \cap \Omega_s} \lambda \cdot \left(v_f - \frac{\partial u}{\partial t}\right) d\gamma = 0. \tag{16}$$

The Lagrange multipliers λ can be interpreted as the normal forces of the fluid acting on the solid. This is exploited in the following iterative scheme, which we use to solve the fully coupled FSI problem:

Step 1 Solve fluid problem (10) on structured grid with Chorin predictor and condition (16).

Step 2 Transfer velocity values v_f and pressures p_f to the unstructured solid grid using L^2-projections P_s^f and $\widehat{P}_s^f$.

Step 3 Reconstruct the fluid forces acting on the solid using fluid pressure and fluid velocities.

Step 4 Solve solid problem.

Step 5 Check convergence of the whole FSI-problem. If convergence is satisfactory, STOP. Otherwise go to the next step.

Step 6 Transfer solid velocity values $\frac{\partial u}{\partial t}$ with P_f^s to fluid grid. GO TO step 1.

2.4 Nonsmooth Multilevel Method

The third application uses the L^2-projection as an interpolation operator in an adapted nonsmooth multilevel method, an extension of the multigrid method. The multigrid method itself (Fedorenko 1962, Hackbusch 2013) is the most efficient method for solving linear elliptic problems such as linear elasticity.

Figure 4 (left) shows the setup of a 3-level multigrid cycle: Roughly speaking, the equation $Au = f$ is partially solved or smoothened at the different levels $l = 0,1,2$, each with their own stiffness matrix A_l (the convention is $A_2 := A$). The corrections c_l of the different levels are linked with the interpolation operators I_{l-1}^l and the principle of multigrid is, that the smoothers on each level are particularly suited for a specific part of the solution spectrum. For optimal convergence the multigrid method requires a nested hierarchy of function spaces, which are usually obtained by successively refining the coarse grid on level 0. The stiffness matrices are usually not assembled on each level by quadrature, but instead by Galerkin assembly in the form of $A_{l-1} := (I_{l-1}^l)^t A_l (I_{l-1}^l)$.

For the simulation of contact in rock fractures, the classic multigrid method is not applicable. We have seen earlier, that the nonpenetration constraints induce a nonlinearity. Furthermore, we usually cannot create a hierarchy of nested spaces by refining a simple coarse grid. Instead we have to coarsen a complex fine grid geometry of a fractured rock, which is virtually impossible. However, we can generate a hierarchy of nested spaces using L^2-projections: We create a simple shape with grid $\mathcal{T}_0$ on the domain Ω that overlaps the fine grid $\mathcal{T}_L$ and refine the simple shape to get successively more refined grids $\mathcal{T}_l, l = 1, .., L-1$. We then compute the L^2-projection operators P_{l-1}^l from 2.1 for every $l = 1, \dots, L$ from the finite element space S_l on $\mathcal{T}_l$ to S_{l-1}on $\mathcal{T}_{l-1}$ such that

$$\int_\Omega (P_{l-1}^l u_l - u_l) v_{l-1} \, d\omega = 0. \tag{17}$$

Again we generate the coarse grid stiffness matrices A_l, $l = 1, .., L-1$ with Galerkin assembly. We like to emphasize here that using this scheme, on the coarser levels we are no longer solving the problem on the finite element space S_{l-1}, but on the image $P_l(S_l) \subset S_{l-1}$. To overcome the inherent nonlinearity of the problem, we employ a nonlinear Gauss-Seidel smoother on the fine grid and we apply solution dependent updates on P_{l-1}^l to ensure the corrections from the coarser grids do not violate the constraints on the fine grid (compare Figure 3, left and right). This leads to a method which can be seen as a hybrid of the monotone multigrid method by Krause (2001), Kornhuber and Krause (2001) and the semigeometric multigrid method described in Dickopf and Krause (2009). It does not require regularization of the contact constraints such as penalty methods and combines global convergence, robustness and multigrid efficiency with the versatility of the L^2-projection.

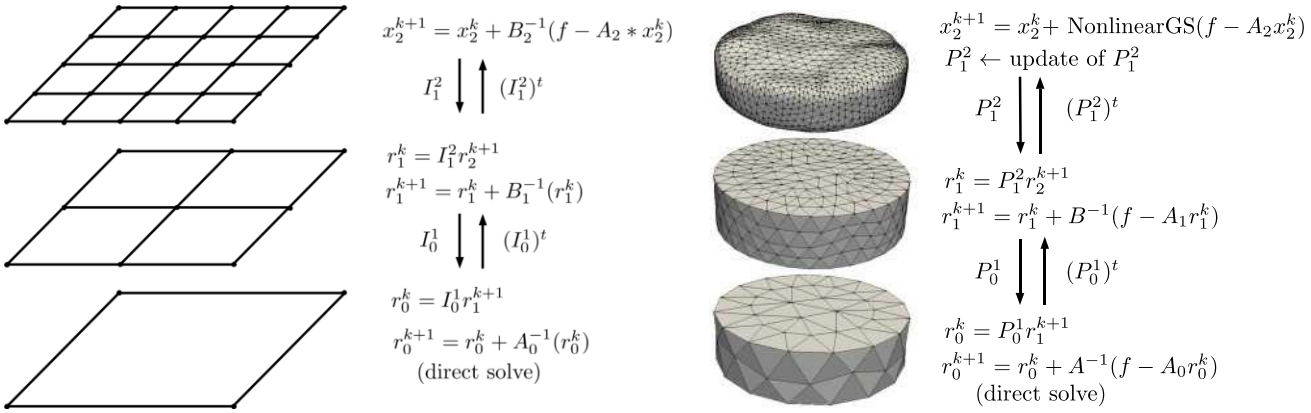

Figure 4: Left: Classic multigrid setup. Right: Setup of nested multilevel hierarchy in nonsmooth multilevel method.

3 IMPLEMENTATION

We have implemented the contact problem and the fluid structure interaction in the MOOSE framework (Gaston et al. 2009), using PETSc (Balay et al. 2015) for the parallel computations of the non-smooth multilevel method. The assembly of the variational transfer operator or L^2-projections uses MOONoLith (Krause and Zulian 2016) (http://moonolith.inf.usi.ch).

4 RESULTS

4.1 Contact

We conducted two numerical experiments for the contact problem: (1) Hertzian contact in order to validate the approach; and (2) emulating a laboratory experiment with two rock fracture surfaces in contact under an increasing normal confining pressure. In the second simulation we investigate if our contact method scales in regards to increased complexity of the surface geometry and whether we can replicate the qualitative behavior of the laboratory experiment. Among the distinct characteristics of the laboratory experiment are the commonly observed, nonlinear closing behavior of a fracture under increasing load (Bandis, Lumsden, and Barton 1983; Zangerl et al. 2008; Vogler et al. 2018) and the development of localized stresses around the asperities (i.e., small scale roughness on a solid body surface) and on the surface.

Hertzian contact is a classic obstacle problem with an existing analytical solution. A sphere, or half sphere in our case, is pushed into a flat plane (see Figure 5, left). A reliable contact method has to be able to replicate the characteristic parabolic shape of the contact stresses, which is the case for our approach (see Figure 5, right).

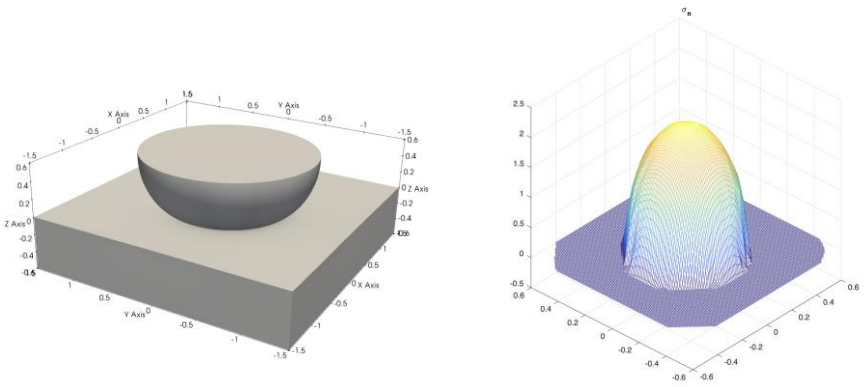

Figure 5: Hertzian contact problem. Left: Setup of the Hertzian contact problem, showing a half-sphere which is pressed into a flat surface. Right: Contact stress distribution.

In the second numerical experiment, we simulate contact between two rough rock fracture surfaces. The fracture (i.e. crack, discontinuity) is situated in a cylindrical specimen (diameter 122mm), with the normal vector of the fracture plane being parallel to the cylinder axis (Figure 6). The bottom of the specimen is fixed in the z-direction, while stresses are applied to the top surface of the specimen, in order to generate contact stresses in the fracture. Specifically, the confining normal stresses for these simulations range from 1 to 20 MPa. The meshes themselves were generated from high resolution fracture surface scans of granitic rock specimen from the Grimsel test site in Switzerland, which were previously employed for laboratory experiments (see Vogler et al. 2016b, 2018). As material parameter we choose a Poisson ratio of 0.33 and a Young`s modulus of 10^7.

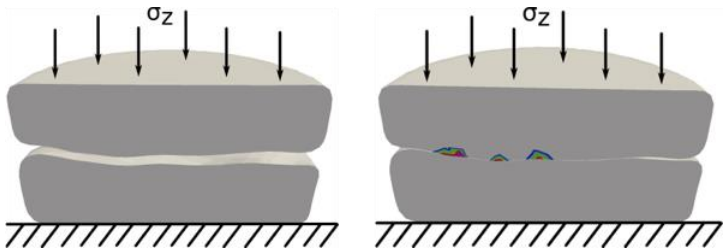

Figure 6: Problem setup for a fractured rock specimen with loading stresses σ_Z applied normal to the rock fracture: Left: Cross section of unloaded specimen ($\sigma_Z = 0$) with a completely open fracture. Right: Cross section of loaded specimen, with local contact stresses shown.

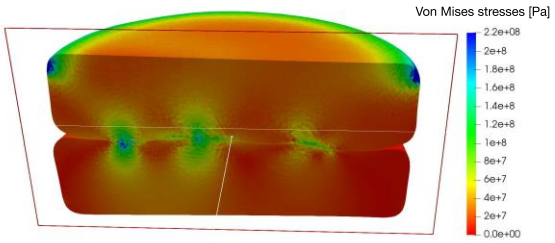

Figure 7: Von Mises stresses generated in the specimen for 4 MPa normal load.

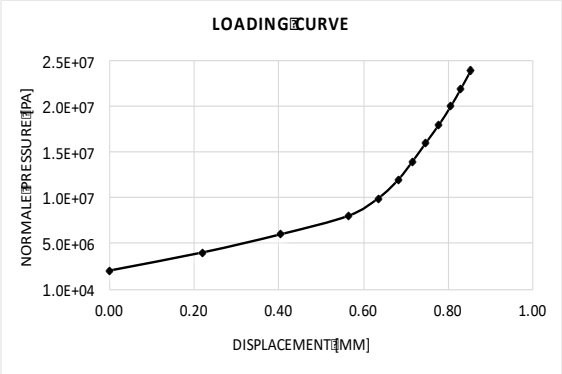

Figure 8: Simulated loading curve, indicating nonlinear displacement relative to normal load.

Figure 6 shows the von Mises stresses on a cross section of the two specimen halves subjected to a confining pressure of 4 Mpa. The two fracture surfaces are partially in contact, while the fracture is still opened (i.e., high aperture or gap) over a large part of the boundary. Although the two meshes are nonmatching at the contact boundary, the two specimen halves do not intersect as is to be expected.

Figure 8 depicts the loading curve, which is showing the characteristic, nonlinear closure behavior commonly observed for rock fractures under normal load (Bandis, Lumsden, and Barton 1983; Zangerl et al. 2008; Vogler et al. 2018). Initially, the fracture closes rapidly for low increases in confining stress, as the fracture only has few contact points which do not offer strong resistance to further closure. As the fracture closes further, an increasingly larger area of the fracture is already in contact, which offers a stronger resistance to closure and leads to the nonlinear closure behavior that can be seen in Figure 8. The curve appears to roughly consists of two linear curves, indicating that the fracture is in full quasi contact at a confining pressure of 10 Mpa, after which it shows the behavior of a single linear elastic body.

Figure 9 shows the apertures on the slave side (of the fracture surface), i.e. the contact boundary of the upper rock. In the top row we see how the gap closes under increased confining pressures of 2,10, and 20 Mpa. Figure 10 shows how the contact stresses gradually developing over a larger and larger surface area, replicating qualitatively the experiments in Vogler et al. (2016b, 2018).

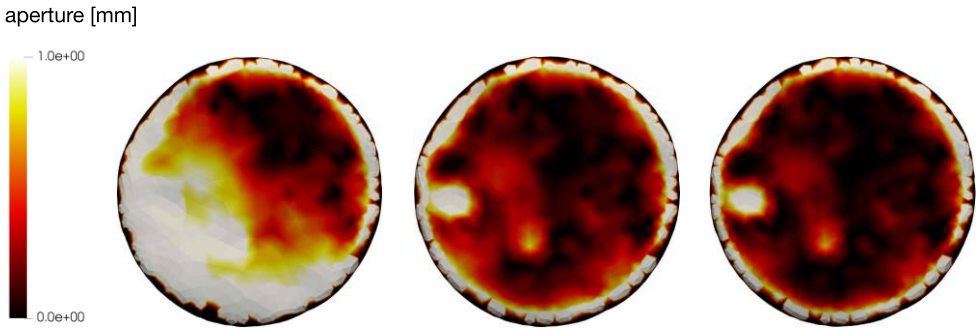

Figure 9: Aperture fields. View on the lower fracture surface for confining stresses of 2, 10 and 20 Mpa.

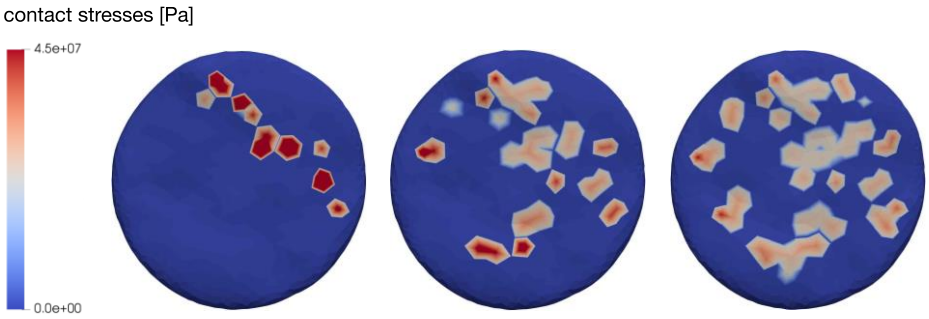

Figure 10: Normal stresses σ_n at 2,10 and 20Mpa.

4.2 Fluid Flow

For the simulation of water flow through a fracture, we cut out two quadratic pieces out of the rock geometry for the solid grid (Figure 3, right) which we used for the contact problem. This is convenient, as we want to embed the solid into the structured fluid grid which is a cuboid (Figure 3, left). In principle, we could also choose a (larger) structured fluid grid which encloses the two rocks completely, however it is more convenient to cut out cuboid piece. It saves computational effort by reducing the overall size of the simulation and it is easier to set up that simulation such that the water flows through the fracture and not around it.

To do so, we apply a fluid velocity of $(1,0,0)^t$ on the left, while setting the velocity constraints to zero on all but the right side and thus initiate a flow from the left to the right. The setup is depicted in Figure 11, which shows a lateral cross section through the rock (grey, opaque) with the fluid flow (yellow, red). On the right in Figure 1 we have visualized partially the flow through the rock. For the visualization we chose a small sphere within the fracture and then visualized the trajectories of the fluid going through this sphere. The visualization shows that the fluid flow in the uniform fluid grid follows very accurately the rough fracture surfaces in the unstructured grid.

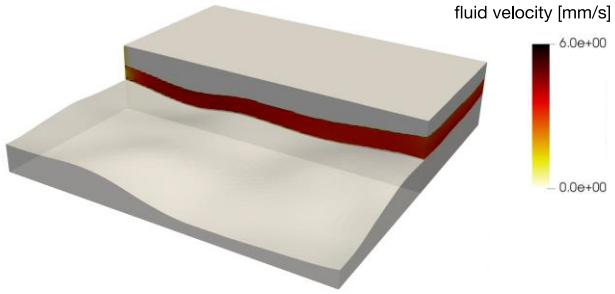

Figure 11: Cross section of through the open fracture showing the setup of the flow simulation.

In the second simulation use a rock geometry of a contact problem when the confining pressure is 2 Mpa, a pressure at which the two solid plates have already formed regions of contact (Figure 12 left).

We then set the internal fluid pressure to 1 Mpa and the fluid velocity to zero, in order to observe the elastic behavior within the fracture under high fluid pressure. On the right in Figure 12 we see a cross section through the fracture, after the pressure has been applied and we can observe how the fluid pressure acts on the solid near the contact areas, leading to small opening displacements.

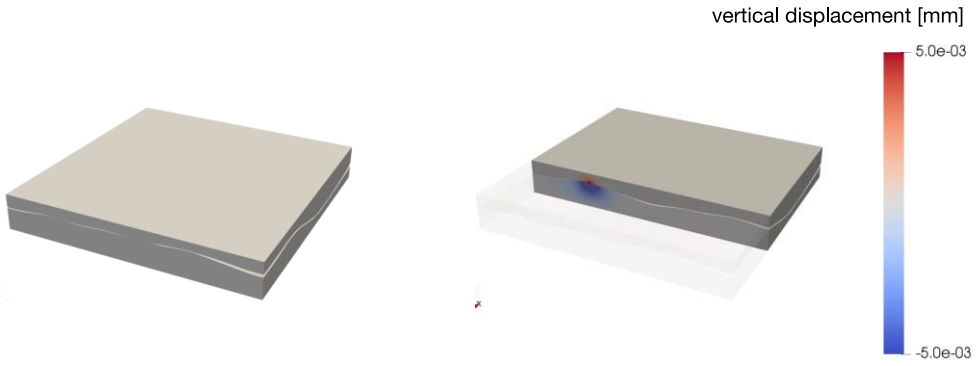

Figure 12: Simulation with a closed fracture. Left: The two rocks plates after being forced into contact. Right: Displacement in z-direction within the fracture, caused by high fluid pressures, which lead to fracture opening.

4.3 Solving with nonsmooth multilevel method

We tested the nonsmooth multilevel method with two obstacle problems. For benchmarking we used a cube with flat surfaces and successive refinements (Figure 13) and for testing the nonsmooth multilevel method with a rock geometry, we used a geometry meshed from a granite sample from the Grimsel test site.

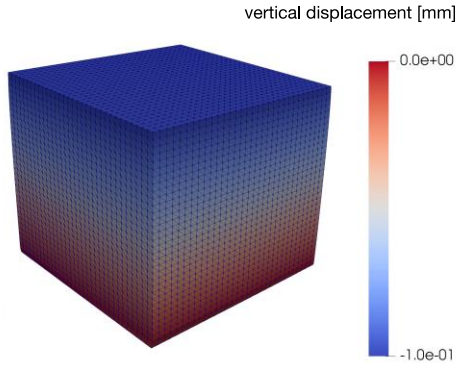

Figure 13: Benchmarking problem. A cube is displaced by 0.3mm into the direction of the z-axis, where it collides with the z-plane.

The benchmarking problem consisted of an obstacle problem with a cube, which we pressed into a planar obstacle in the z-plane by enforcing a movement in normal direction via Dirichlet boundary conditions. The number of levels and degrees of freedom (dof) is increased by successive refinement of the finest grid. Here, we were interested in the convergence behavior in relation to the number of iterations and in relation to the parallelization, i.e. the number of processes used. The convergence criterion is the step length, i.e. $\| \text{step} \| = \| \mathbf{x}_{k=1} - \mathbf{x}_{k=1} \|$ to a tolerance of 10^{-12}. The left side of figure 14 shows the convergence of an obstacle problem with 2 levels with 1'107 dof, 3 levels with 7'395 dof, 4 levels with 53'955 dof and 5 levels with 412'035 dof.

We observe that after the first 4 iterations convergence becomes linear, since the nonsmooth multiscale method operates like a multigrid algorithm after the contact boundary is identified. For every new refinement (i.e. additional level), about 10 additional multigrid iterations are required. The right side of figure 14 shows a scaling experiment of the test problem with 2'147'076 degrees of freedom from 4 to 30 processes indicating good strong scaling behavior.

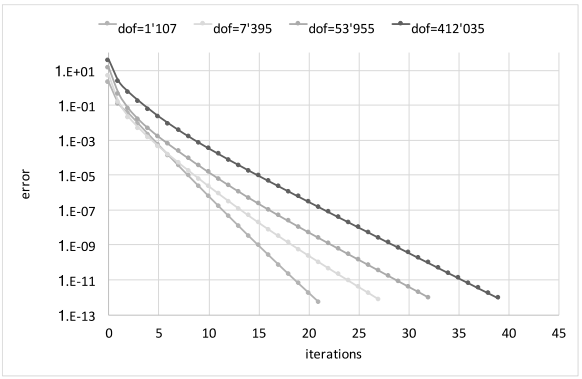

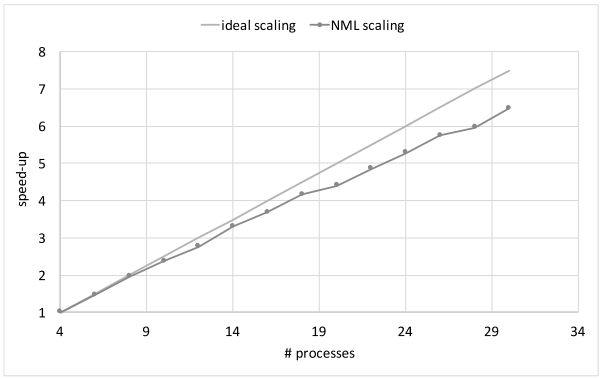

Figure 14: Left: Convergence of the non-smooth multilevel method. Right: Strong scaling experiment.

For the second simulation we wanted to prove the feasibility of the semigeometric multigrid concept with complex geometries. We took a geometry meshed from an actual rock sample and created a nested multilevel hierarchy using the approach outlined in section 2.4. Figure 15 (left) shows the rock geometry on the left and the enclosing coarse grids in the middle and on the right. The middle grid was obtained by refining the coarsest grid on the right. Note that on the left in Figure 15 we show coarser geometries than were actually used, in order to illustrate the setup more clearly. On the right in Figure 15 we show the simulated rock body after solving the contact problem with the nonsmooth multilevel method. The plane in which the rock is in contact is not shown here, for the sake of better visualization of the fine refinement.

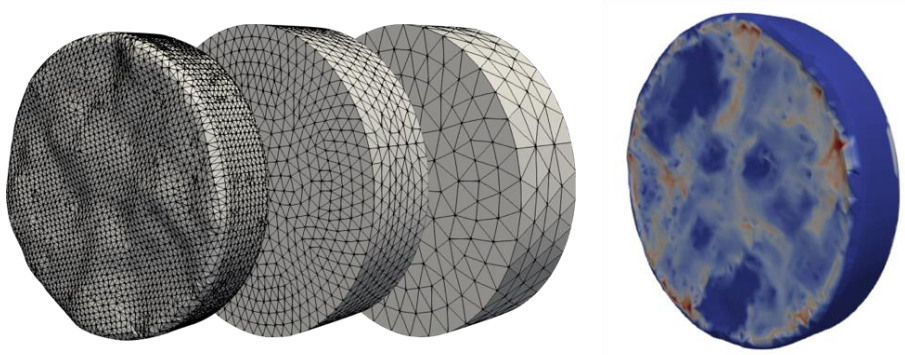

Figure 15: Left: Multilevel hierarchy for rock specimen geometry. The original geometry is shown on the far left, with increasingly coarser grid representations of the geometry to the right. Right: Simulation of a rock fracture in contact. Red color indicates contact.

This shows that the nonsmooth multilevel method shown here is both scalable and applicable to contact problems with complex geometries which will enable us to scale up contact simulations significantly in the future.

5 CONCLUSIONS

A generic transfer operator was used to transfer information between different mesh grids for three applications: (1) A contact problem between two solid bodies with rough surfaces; (2) 3D fluid flow simulation between two bodies with rough surfaces and fluid structure interaction; and (3) a hierarchic multilevel approach to enable simulations of very large contact problems.

The Mortar approach using L^2-projections enables high-resolution simulations of the mechanical behavior of two fracture surfaces in contact. Our presented approach is validated with existing analytical solutions and applied to real world application scenarios. Specifically, the mechanical contact of two rough rock fractures is solved for increasing confining pressure, where the characteristic fracture closure behavior observed in numerous studies is captured.

We then used the L^2-projections to solve an FSI problem, which is of particular importance to capture processes commonly encountered in reservoir engineering. We applied an immersed boundary type approach in which the rock, modelled on an unstructured grid, was embedded in the structured mesh for the fluid problem. For the coupling we used L^2-projections to transfer the fluid velocities and pressure between the fluid and the solid grid. We were able to simulate water flow inside the fracture and displacement of the rock along the fracture.

Finally, we have shown that using L^2-projections we were able to construct nested multilevel hierarchy for complex geometries to solve the obstacle problem with the nonsmooth multilevel method. The method is globally convergent and does not require further regularization such as penalty methods. This enables us to solve the contact problem with multigrid efficiency and to massively scale up the problem size.

Acknowledgements

We gratefully acknowledge funding by the Swiss Competence Center for Energy Research - Supply of Electricity (SCCER-SoE).

REFERENCES

Baaijens, F. P. T., A Fictitious Domain/Mortar Element Method for Fluid–Structure Interaction, *International Journal for Numerical Methods in Fluids*, **35** (7), John Wiley & Sons, Ltd., (2001), 743–61.

Satish, B., and Abhyankar S., and Adams, M. F., and Brown, J., and Brune P., and Buschelman, K., and, Dalcin, L. et al., PETSc Users Manual., *ANL-95/11 - Revision 3.6. Argonne National Laboratory*, http://www.mcs.anl.gov/petsc, (2015).

Bandis, S.C., A.C. Lumsden, and N.R. Barton, Fundamentals of Rock Joint Deformation, *International Journal of Rock Mechanics and Mining Sciences & Geomechanics*, **20** (6), (1983), 249–68.

Barton, N., S. Bandis, and Bakhtar, K., STRENGTH, Deformation and Conductivity Coupling of Rock Joints, *International Journal of Rock Mechanics and Mining Sciences*, **22** (3), (1985), 121–40.

Bernardi, C., A new nonconforming approach to domain decomposition: the mortar element method. Nonlinear partial equations and their applications, Pitman, (1989).

Bernardi, C. and Maday, Y. and Rapetti, F., Basics and some applications of the mortar element method.", *GAMM-Mitteilungen*, **28**(2), (2005), 97–123.

Brown, S. R., FLUID-Flow Through Rock Joints - the Effect of Surface-Roughness, *Journal of Geophysical Research-Solid Earth and Planets*, **92** (B2), (1987), 1337–47.

Dickopf, T., and Krause, R., Efficient Simulation of Multi-Body Contact Problems on Complex Geometries: A Flexible Decomposition Approach Using Constrained Minimization, *International Journal for Numerical Methods in Engineering*, John Wiley & Sons, Ltd., **77**(13), (2009), 1834–62.

Fedorenko, R. P., A Relaxation Method for Solving Elliptic Difference Equations, *USSR Computational Mathematics and Mathematical Physics*, Elsevier, 1 (4), (1962), 1092–6.

Gaston, D., Newman, C., Hansen, G., and Lebrun-Grandié, D., MOOSE: A Parallel Computational Framework for Coupled Systems of Nonlinear Equations, *Nuclear Engineering and Design*, 239, (2009), 1768–78.

Hackbusch, W., Multi-grid methods and applications, volume 4. Springer Science & Business Media, (2013).

Hesch, C., Gil, A.J., Arranz, A. Carreño, Bonet, J., and Betsch, P., A Mortar Approach for Fluid–Structure Interaction Problems: Immersed Strategies for Deformable and Rigid Bodies, *Computer Methods in Applied Mechanics and Engineering*, **278**, Elsevier, (2014), 853–82.

Hintermüller, M., Kazufumi I., and Kunisch, K., The Primal-Dual Active Set Strategy as a Semismooth Newton Method, *SIAM Journal on Optimization*, **13** (3), SIAM, (2002), 865–88.

Jiang, Y., Li, B., and Tanabashi, Y., Estimating the Relation Between Surface Roughness and Mechanical Properties of Rock Joints, *International Journal of Rock Mechanics and Mining Sciences*, **43** (6), (2006), 837–46.

Kikuchi, N., and Oden, J., Contact Problems in Elasticity: A Study of Variational Inequalities and Finite Element Methods, SIAM, (1988).

Kornhuber R., and Krause, R., Adaptive multigrid methods for Signorinis problem in linear elasticity, *Computing and Visualization in Science*, **4**(1):9–20, (2001).

Krause, R., A Nonsmooth Multiscale Method for Solving Frictional Two-Body Contact Problems in 2D and 3D with Multigrid Efficiency, *SIAM Journal on Scientific Computing*, **31** (2), (2009), 1399–1423.

Krause, R., Monotone Multigrid Methods for Signorini's Problem with Friction, PhD thesis, Freie Universität Berlin, (2001).

Krause, R., and Zulian, P., A Parallel Approach to the Variational Transfer of Discrete Fields Between Arbitrarily Distributed Unstructured Finite Element Meshes, *SIAM Journal on Scientific Computing*, **38** (3):C307–C333, (2016).

Matsuki, K., Wang, E.Q., Giwelli, A.A., and Sakaguchi, K., Estimation of Closure of a Fracture Under Normal Stress Based on Aperture Data, *International Journal of Rock Mechanics and Mining Sciences*, **45** (2), (2008), 194–209.

McClure, M. W., and Horne, R. N., Correlations Between Formation Properties and Induced Seismicity During High Pressure Injection into Granitic Rock, *Engineering Geology*, **175**, (2014), 74–80.

Nemoto, K., Watanabe, N., Hirano, N., and Tsuchiya, N., Direct Measurement of Contact Area and Stress Dependence of Anisotropic Flow Through Rock Fracture with Heterogeneous Aperture Distribution, *Earth and Planetary Science Letters*, **281** (1-2), (2009), 81–87.

Nestola, M., Becsek, B., Zolfaghari, H., Zulian, P., Obrist, D., and Krause, R. (2017), An Immersed Boundary Method Based on the Variational L2-Projection Approach, *Proceedings DD24 2016*, (2017).

Park, H., Osada, M., Matsushita, T., Takahashi, M. and Ito, K., Development of Coupled Shear-Flow-Visualization Apparatus and Data Analysis, *International Journal of Rock Mechanics and Mining Sciences*, **63**, (2013), 72–81.

Pyrak-Nolte, L. J., and Morris, J. P., Single Fractures Under Normal Stress: The Relation Between Fracture Specific Stiffness and Fluid Flow, *International Journal of Rock Mechanics and Mining Sciences*, **37** (1-2), (2000), 245–62.

Rutqvist, J., and Stephansson, O., The Role of Hydromechanical Coupling in Fractured Rock Engineering, *Hydrogeology Journal*, **11** (1), (2003), 7–40.

Tatone, B. S. A., and Grasselli, G., Characterization of the Effect of Normal Load on the Discontinuity Morphology in Direct Shear Specimens Using X-Ray Micro-Ct, *Acta Geotechnica*, **10** (1), (2015), 31–54.

Tester, J. W., Anderson, Batchelor, B., A., Blackwell, D., DiPippo, R., Drake, E., Garnish, J., et al., The Future of Geothermal Energy: Impact of Enhanced Geothermal Systems (EGS) on the United States in the 21st Century, Massachusetts Institute of Technology 209, (2006).

Vogler, D., Amann, F., Bayer, P., and Elsworth, D., Permeability Evolution in Natural Fractures Subject to Cyclic Loading and Gouge Formation, *Rock Mechanics and Rock Engineering*, **49** (9), (2016), 3463–79.

Vogler, D., Settgast, R. R., Annavarapu, C., Bayer, P., and Amann, F., Hydro-Mechanically Coupled Flow Through Heterogeneous Fractures, *PROCEEDINGS, 42nd Workshop on Geothermal Reservoir Engineering*, Stanford, CA SGP-TR-209, (2016b).

Vogler, D., Settgast, R. R., Annavarapu, C., Madonna, C., Bayer, P. and Amann, F., Experiments and Simulations of Fully Hydro-Mechanically Coupled Response of Rough Fractures Exposed to High Pressure Fluid Injection, *Journal of Geophysical Research: Solid Earth*, 123, (2018).

Vogler, D., Walsh, S. D. C., Bayer, P. and Amann, F., Comparison of Surface Properties in Natural and Artificially Generated Fractures in a Crystalline Rock, *Rock Mechanics and Rock Engineering*, **50** (11), (2017), 2891–2909.

Wohlmuth, B., and Rolf, H., Monotone Multigrid Methods on Nonmatching Grids for Nonlinear Multibody Contact Problems, *SIAM Journal on Scientific Computing***, 25**, (1), (2003), 324–47.

Yu, X., and Vayssade, B., Joint Profiles and Their Roughness Parameters, *International Journal of Rock Mechanics and Mining Sciences & Geomechanics*, Pergamon, **28**, (1991), 333–36. 4

Zangerl, C., Evans, K. F., Eberhardt, E., and Loew, S., Normal Stiffness of Fractures in Granitic Rock: A Compilation of Laboratory and in-Situ Experiments, *International Journal of Rock Mechanics and Mining Sciences*, **45** (8), (2008), 1500–1507.

Zimmerman, R. W., Kumar, S., and Bodvarsson, G. S., Lubrication Theory Analysis of the Permeability of Rough-Walled Fractures, *International Journal of Rock Mechanics and Mining Sciences and Geomechanics*, **28** (4), (1991), 325–31.